Appl Phys A (2008) 92: 939–943
DOI 10.1007/s00339-008-4607-y

Applied Physics A
Materials Science & Processing

Interaction of short laser pulses with metals at moderate intensities

S.I. Anisimov · N.A. Inogamov · Yu.V. Petrov · V.A. Khokhlov · V.V. Zhakhovskii · K. Nishihara · M.B. Agranat · S.I. Ashitkov · P.S. Komarov

Received: 12 October 2007 / Accepted: 9 April 2008 / Published online: 28 May 2008

Abstract The developed model including hydrodynamics with electron heat conduction and electron–ion energy exchange, and cavitation breakup of stretched metastable liquid aluminum (Al) is compared with our laser experiments. For the first time the measured and calculated ablation thresholds agree well in both crater depth and fluence.

PACS 79.20.Ds · 61.43.Bn · 02.70.Ns

The ultrashort laser–matter interaction at incident fluence $F_{\text{inc}} \sim 1\ \text{J/cm}^2$ is important for fundamental physics and for industrial applications [1–5]. The interaction is complicated because it is a result of interplay of the following component processes: (i) absorption of incident radiation by electrons, (ii) electron heat conduction of absorbed energy from surface to the bulk of the target, (iii) cooling of electrons due to electron–ion energy exchange, and (iv) cavitation breakup of stretched metastable liquid metals. To describe the processes (i)–(iii) we have developed a numerical two-temperature hydrodynamical (2T-HD) model. The molecular dynamics (MD) approach is ideally appropriate for detailed simulation of nucleation kinetics in process (iv). The 2T-HD model is based on the well-known model [6] of electron–ion energy exchange in condensed matter [1–3, 5]. The extended model includes hydrodynamic terms (see also [3]). The model equations are

$$\begin{aligned} &\rho_t + (\rho u)_x = 0, \qquad \rho u_t + \rho u u_x + p_x = 0, \\ &E^{\text{e}}_t + u E^{\text{e}}_x = -p^{\text{e}} u_x + \left(\kappa T^{\text{e}}_x\right)_x - \alpha\left(T^{\text{e}} - T^{\text{i}}\right) + S, \qquad (1) \\ &E^{\text{i}}_t + u E^{\text{i}}_x = -p^{\text{i}} u_x + \alpha\left(T^{\text{e}} - T^{\text{i}}\right), \end{aligned}$$

where subscripts t, x mean differentiation with respect to time and coordinate, and superscripts e, i indicate electron and ion subsystem, correspondingly. The total pressure is $p = p^{\text{e}} + p^{\text{i}}$. We choose Al as an example of typical metal, which has well-established thermodynamical and optical data as well as accurate interatomic potential for MD simulation [7]. The coefficients of electron heat conduction κ and electron–ion energy exchange α for Al are taken as in [5]. For our fluences the displacement of matter over a pump laser pulse duration $\tau_{\text{L}} = 0.1$ ps is much smaller than the skin depth in Al. Therefore the smoothing of the boundary density jump due to motion has no effect on the laser absorption described by a term S in the electron energy balance equation. The internal ion energy and pressure E^{i}, p^{i} are taken from the wide-range equation of state [8]. Electron components of energy and pressure E^{e}, p^{e} are evaluated by Fermi formulae [2, 3] so that they have the quadratic form $(E^{\text{e}}, p^{\text{e}}) \propto (T^{\text{e}})^2$ near Fermi energy E_{F} and pressure p_{F} for the low temperatures $T^{\text{e}} \ll E_{\text{F}}$. In the opposite case of $T^{\text{e}} \gg E_{\text{F}}$ the energy and pressure E^{e}, p^{e} approach the nondegenerate ideal gas quantities asymptotically [2, 3].

For the fluence near ablation threshold $F \sim F^{\text{abl}}$, the time evolution may be divided into two consecutive stages: the two-temperature (2T) and one-temperature (1T) stage. In the

---

S.I. Anisimov · N.A. Inogamov (✉) · Yu.V. Petrov · V.A. Khokhlov
L.D.Landau Institute for Theoretical Physics RAS, Chernogolovka 142432, Russia
e-mail: nailinogamov@googlemail.com

V.V. Zhakhovskii · K. Nishihara
Institute of Laser Engineering, Yamada-oka 2-6, Suita, Osaka 565-0871, Japan

V.V. Zhakhovskii · M.B. Agranat · S.I. Ashitkov · P.S. Komarov
Joint Institute of High Temperature RAS, 13/19 Izhorskaya street, Moscow 125412, Russia

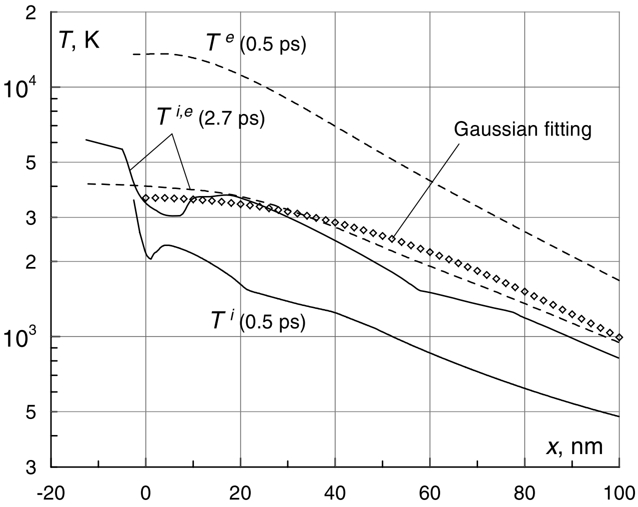

Fig. 1 The temperature profiles of electron and ion subsystems for different times within 2T stage. Initially $T^{\mathrm{e}} \gg T^{\mathrm{i}}$. At $t = 0$ the position of target-vacuum boundary is $x = 0$

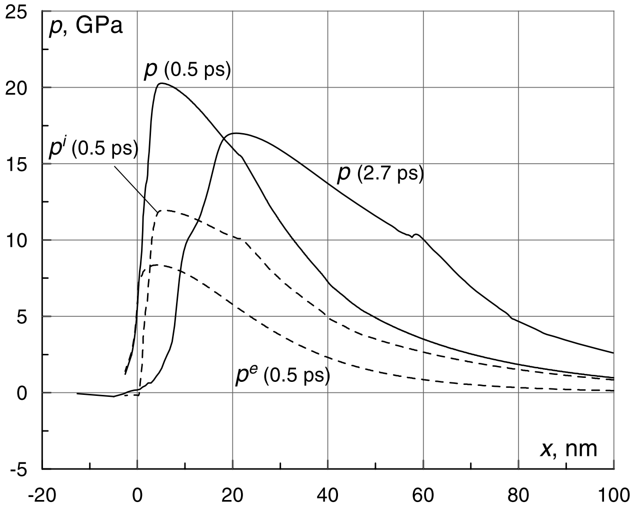

Fig. 2 The reflection of a high pressure sonic signal from vacuum boundary and the decreasing of electron temperature results in the drop of total pressure during 2T stage

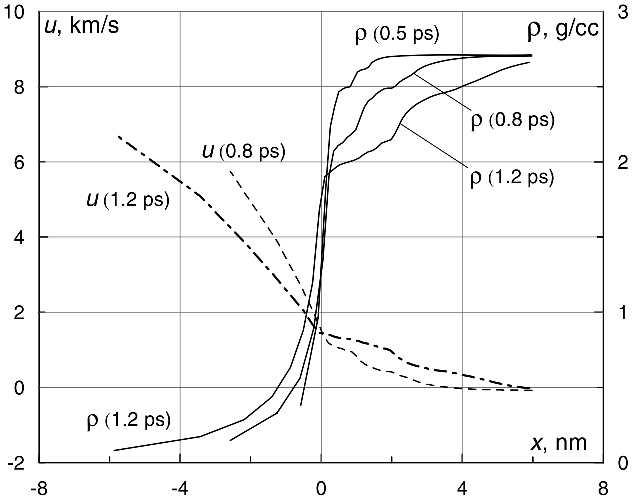

Fig. 3 Density (*solid lines*) and flow velocity (*dash lines*) profiles for the different times in 2T stage

beginning of the 2T stage the electron thermal energy and temperature $E^{\mathrm{e}}, T^{\mathrm{e}}$ are much larger than $E^{\mathrm{i}}, T^{\mathrm{i}}$ within the heated layer. As thermal wave penetrates into the target, the T^{e} decreases and the T^{i} increases. The 2T stage is completed when the temperatures T^{e} and T^{i} become equal. The heat capacity of electrons is substantially below the heat capacity of ions for $T^{\mathrm{e}} \ll T_{\mathrm{F}}$ [2, 3], where $T_{\mathrm{F}} = 115$ kK for Al. Since then $T^{\mathrm{e}} \approx T^{\mathrm{i}} = 2$–4 kK, the electron energy E^{e} goes down to 10–20% of the ion energy.

Figure 1 presents the temperature distributions T^{e} and T^{i} in the intermediate point of time $t = 0.5$ ps and the final point $t = 2.7$ ps of 2T stage for the case of absorbed fluence $F_{\mathrm{abs}} = 70\ \mathrm{mJ/cm^2}$. The time is reckoned from the maximum of pump laser intensity $I(t) \propto \exp(-t^2/\tau_{\mathrm{L}}^2)$, where the duration of laser pulse is $\tau_{\mathrm{L}} = 0.1$ ps. Figure 1 shows that the thickness of heated layer d_{h} (measured at half-height of T^{i} profile in dense matter) increases from $d_{\mathrm{h}} = 40$ nm at the time 0.5 ps to $d_{\mathrm{h}} = 55$ nm at 2.7 ps. The temperature difference $(T^{\mathrm{e}} - T^{\mathrm{i}})$ decreases with time, and transition between 2T and 1T stages occurs within time slice 2–3 ps. For moderate fluences 2T hydrodynamical effects are small in total mass and energy balances as discussed later in the article. Therefore temperatures $T^{\mathrm{e}}, T^{\mathrm{i}}$ outside of rarefaction zone are in close agreement with those obtained in 2T motionless model [2]. In the early time of 1T stage the Gaussian curve can be used in fitting of the ion temperature profile as shown by Fig. 1. This approximation provides an initial temperature profile for our MD simulations.

For fluences $F \sim F^{\mathrm{abl}}$ the electron pressure p^{e} is significant factor within 2T stage. The pressure profiles p^{e}, p^{i}, $p = p^{\mathrm{e}} + p^{\mathrm{i}}$ at the instants 0.5 and 2.7 ps are shown in Fig. 2. Initially the total pressure is high, and it results in higher expansion rate in 2T stage when compared with 1T stage. The decreasing of total pressure with time $t = 0.5$–2.7 ps is not only associated with the reflection of sonic wave from vacuum boundary, but with fast cooling of electrons by heat conduction and electron–ion energy exchange as well. The electron pressure p^{e} becomes a minor part of the total pressure $p \approx p^{\mathrm{i}}$ after $t = 2.7$ ps.

Figure 3 gives the calculated profiles of density and velocity of Al target for the fluence $F_{\mathrm{abs}} = 70\ \mathrm{mJ/cm^2}$. The critical electron density n_{c} at the critical surface $x_{\mathrm{c}}(t)$ of Al plasma is about two order less than the electron density in solid Al. Hence the surface x_{c} is located within a low density plasma layer near the target (see Fig. 3). The measured speed u_{c} of surface x_{c} is about ∼2–5 km/s within the 2T stage. At the termination of 2T stage this speed drops to

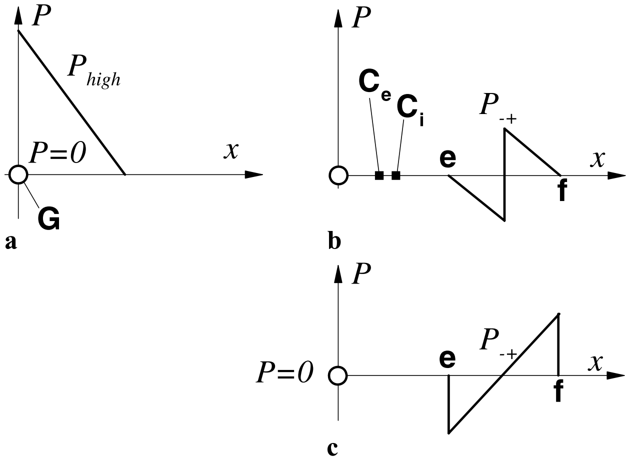

Fig. 4 Hydrodynamic interaction between the initial compressed region p_{high} (**a**) and vacuum boundary G, resulting in formation of the quiet zone $C_{\mathrm{i}}e$ (**b**) or Ge (**c**)

$\sim$1 km/s as hot plasma expands into vacuum, uncovering the slow moving surface of liquid Al (the ablation threshold F^{abl} is significantly higher than the melting threshold, and so Al melts during a few picoseconds). Thus $u_{\mathrm{c}} \sim 1$ km/s in the early 1T stage. Due to very low density and ionization degree of Al vapor for melting temperature, the critical surface coincides with surface of Al melt at the 1T stage.

The speed u_{c} changes with time in the 1T stage. It decreases mainly during the acoustic time $t_{\mathrm{s}} = d_T/c_{\mathrm{s}}$, where d_T is a thickness of the heated layer after the 2T stage. Thus u_{c} decays due to fast dispersion of hot plasma within the 2T stage, while at the 1T stage u_{c} decays as a result of tear resistance of a liquid. For fluences $F < F^{\mathrm{abl}}$ the cohesion force in liquid slows down the speed u_{c} to zero.

According to our calculations the thickness of Al layer ablated as plasma during the 2T stage is a few nanometers (see Fig. 3). This is substantially less than both d_T and crater depth d_{Cr}. Such fact is related to the relatively large electron–ion energy exchange coefficient α in (1) for Al. As an opposite example, gold has much smaller α, and the mass of ablated gold in the 2T stage is comparable with the substance removed in the 1T stage.

To study cavitation the continuum hydrodynamics must be supplemented by a semi-phenomenological model of nucleation kinetics. Models of this type incorporate a number of phenomenological parameters obtained from experimental data. The MD simulation is free from such parameters. These phenomenological parameters depend on the rate of deformation $\dot{V}/V$. They vary over a wide range according to different experimental conditions. The rate $\dot{V}/V$ is determined by spatial and temporal features of the experiment, since $\dot{V}/V \sim v/l \sim M/t_{\mathrm{s}}$, where l is the thickness of expanding layer, v is the expansion velocity, $M = v/c_{\mathrm{s}}$. The rate of deformation is relatively small in experiments with ion beams or high explosives, where the thickness $l \sim 1$ mm is large. At the moment the extremely high rate of deformation is realized in the experiments using the femtosecond laser pulses being discussed in this report.

That is why the MD method based on atomistic simulation is well suited to study laser ablation accompanied by melting and cavitation. There is an important distinction from the hydrodynamic 2T calculation, namely, the absence of the electron pressure contribution in MD simulation. As have been mentioned above, the high electron pressure forms the fast and hot 2T rarefaction wave at 2T stage. But the kinetic energy and mass of the 2T rarefaction wave is smaller than the kinetic energy and mass involved in motion at advanced 1T stage. For calculations illustrated by Figs. 1, 2, 3, the kinetic energy of expansion $\int (1/2)\rho u^2\, dx \approx 5$ mJ/cm^2 at the time $t = 2.7$ ps. Thus the small part of absorbed fluence $F_{\mathrm{abs}} = 70$ mJ/cm^2 is merely used for acceleration of matter in the 2T rarefaction wave.

We use the MPD^3 algorithm [9] for large-scale parallel MD simulation of Al with EAM potential given by Mishin et al. [7]. At $t = 0$ the motionless target is a perfect Al crystal having a face-centered cubic lattice structure at zero pressure and room temperature. The crystal has a rectangular form with dimensions $l_x \times l_y \times l_z$ and periodical conditions imposed along the y, z-directions. The crystal direction [110] is aligned with x-axis, and $l_x = 689$ nm. The maximal number of atoms in simulation was 76,296,000. The initial temperature $T_0(x)$ plotted by diamonds in Fig. 1 is formed by heating up Al atoms during 1–2 ps by Langevin thermostat with forces $\Xi(x_{\mathrm{i}}) = \xi(x_{\mathrm{i}}) - \beta m_i v_i$, where $\xi(x_{\mathrm{i}})$ is a position-dependent Gaussian random force applied to i-atom with mass m_i and velocity v_i, and β is a friction coefficient. To obtain a prescribed temperature $T(x)$, the variance of distribution $\xi(x_{\mathrm{i}})$ should satisfy the condition $\sigma_i^2 = 2\beta m_i k_{\mathrm{B}} T(x_{\mathrm{i}})/h$. The integration time step was $h = 2$ fs for $T_0 < 4$ kK, and $h = 1$ fs for higher temperatures, and $\beta = 1/200h$ in our MD simulations. Langevin thermostat operated for first 1,000 simulation steps and then shut down. This short heating is assumed to simulate the 2T stage.

To simulate a semi-infinite target we develop a new "acoustic cut-off" procedure. Due to interaction of sound waves with the boundary G as shown in Fig. 4, the triangle pressure profile p_{high} (Fig. 4a) generated by an ultrashort pump transforms to the twofold pulse (Fig. 4b, c) $p_{\pm}$ consisting of stretching p_- and compression p_+ waves. The twofold pulse is a simple Riemann wave propagating rightwards along the characteristics $u + c$.

By the time $\sim t_{\mathrm{s}} = d_T/c_{\mathrm{s}}$ the twofold pulse escapes from the boundary G leaving behind *the quiet zone* $C_{\mathrm{i}}e$ (Fig. 4b) or Ge (Fig. 4c). The quiet zone is formed in both cases, at $F < F^{\mathrm{abl}}$, when Ge segment remains unbroken, as well as at $F > F^{\mathrm{abl}}$, when the cavitation region $C_{\mathrm{e}}C_{\mathrm{i}}$ turns out to be within the Ge zone.

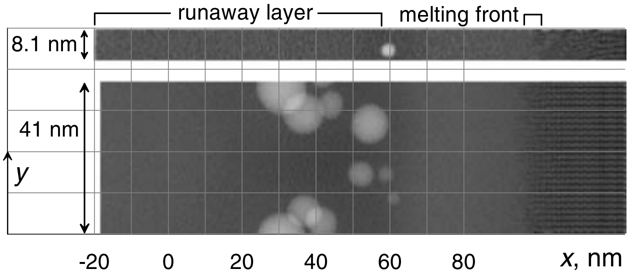

Fig. 5 YZ-cross section size of MD box affects the nucleation processes: YZ-density maps from the small set (s) at $t = 36$ ps and from the large set (L) at $t = 31$ ps. Nucleation is delayed in the narrow MD box. The both MD simulations have the initial surface temperature $T_0(0) = 2{,}620$ K. The pixel blackness is proportional to $\int_0^{l_z} \rho(x, y, z, t)\,dz$

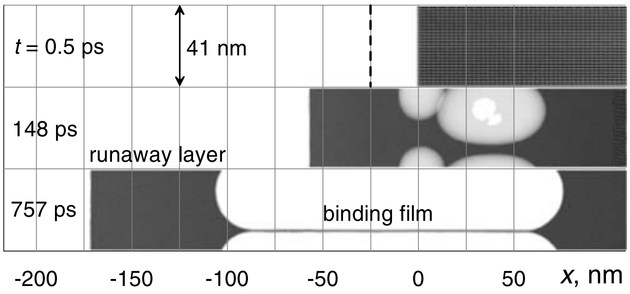

Fig. 6 The stretching of the binding film before its breakup (if $F > F^{\mathrm{abl}}$) or before its contraction (if $F < F^{\mathrm{abl}}$) takes a very long time. The maps from the set (L) as in Fig. 5

In linear acoustics the twofold pulse **ef** has a profile shown in Fig. 4b. The nonlinear effect of focusing of characteristics results in the breaking of compression ($p > 0$) wave p_+, as well as the breaking of stretching ($p < 0$) wave p_- for the particular case $F < F^{\mathrm{abl}}$. These wave breakings induce the shock waves at two points, the first on trailing front of twofold pulse **e** and the second on leading edge of the pulse **f**, see Fig. 4c. In the case $F > F^{\mathrm{abl}}$ the shock wave in point **e** ($p < 0$) is created after appearance of cavitation zone $C_\mathrm{e}C_\mathrm{i}$.

In the "acoustic cut-off" procedure the terminating plane x_t begins to move from the right boundary of target to *the quiet zone* with supersonic velocity at the time t_1, when the trailing front **e** (Fig. 4b, c) propagates a distance $\sim 2d_T$. All atoms to the right of x_t are eliminated from MD simulation. The plane x_t stops at t_2 on the distance $\sim 2d_T$ from the boundary G. After that the free surface condition is established on the right boundary of remained target. During the movement of terminating plane $[t_1, t_2]$ the number of processors is constant, so the simulation time per a step decreases.

Two sets of simulations are made—the set (s) with number of atoms $N \sim 3 \times 10^6$ and small cross section $l_y \times l_z \sim 7 \times 7$ nm^2 of MD box, and the set (L) with $N \sim 76 \times 10^6$ and large cross section $\sim 40 \times 40$ nm^2. The difference between the two sets is clear from Fig. 5. The evaluated ablation threshold is $F^{\mathrm{abl}}_{\mathrm{abs}} = 65$ mJ/cm^2, and the corresponding crater depth is 48 nm for the set (L). The threshold temperature and fluence are 2% higher for the set (s). By contrast, an (30–100)-fold expansion of transverse area qualitatively changes the dynamics of cavitation (Figs. 5, 6). There is a fast $\sim 0.5 t_\mathrm{s}$ detachment of the runaway layer (see Fig. 5) after appearance of a cavitation bubble in the set (s), whereas the runaway process takes many t_s in the set (L).

The surface tension of the binding film slows down the runaway layer. It is found that the decelerating force in MD simulation is equal to $2 l_z \sigma$, where σ is a surface tension coefficient taken from [10]. We have found that the binding film is extremely stretchable as it is illustrated by Fig. 6, where the dash line indicates the position of interface after thermal expansion estimated by formula $\int_0^\infty \alpha_V(T_0(x))[T_0(x) - 300]\,dx \approx 0.25 d_T \approx 25$ nm with thermal coefficient $\alpha_V(T) = (\partial V / V \partial T)_\mathrm{p}$ taken on Al binodal. One can see in Fig. 6 that the displacement of runaway layer $x_\mathrm{r}(t)$ at $t = 757$ ps noticeably exceeds the thermal expansion. This result clarifies the experiments with semiconductors [4] where large surface displacements have been observed. The MD displacement $x_\mathrm{r}(t)$ agrees well with displacements measured at our terawatt laser facility.

The experimental setup is based on the chromium-doped forsterite laser system with pulse duration $\tau_\mathrm{L} = 0.1$ ps, see [3] and references therein. The pump-probe technique at the first (pump) and second (probe) harmonics is applied. For pump incident fluences 0.1–10 J/cm^2 the dynamics of heating and expansion is studied in a wide range of delays (0.1 ps–5 ns) by means of the high accuracy microinterferometric and reflectivity measurements. The ablation of Al starts from the incident fluence $F^{\mathrm{abl}}_{\mathrm{inc}} = 0.74 \pm 0.03$ J/cm^2 measured for p-polarized pulse with inclination 45°. It should be pointed out that, unlike the threshold for incident fluence, the absorbed fluence threshold does not depend on inclination and polarization of the incident pump.

By using the experimentally measured reflectivity we found that the absorbed fluence F_{abs} is only 9% fraction of the incident fluence $F^{\mathrm{abl}}_{\mathrm{inc}}$ on the ablation threshold. Therefore the ablation threshold for absorbed fluence is $F^{\mathrm{abl}}_{\mathrm{abs}} =$ 64–70 mJ/cm^2. This value is in a good agreement with theoretical one presented above. The experiments give the crater depth 50 nm at the threshold, which agrees well with simulation.

Conclusion New experimental results and modeling of ultrashort laser-matter interaction have been presented. (i) Combined 2T and MD models first proposed in [1] for simulation of bulk targets has been extended by including effects of electronic pressure. (ii) Acoustic response on irradiation has been studied and new boundary condition with incoming wave elimination for simulation of bulk target by finite MD system has been developed. Breaking of stretching wave and formation of shock with negative pressure has been found. (iii) Importance of cross-section dimensions of MD box has been demonstrated. Earlier MD results correspond to simulations with a small cross section similar to narrow strip in the upper part of Fig. 5. Simulation with larger S explains the origin of anomalous huge displacements revealed in [4] and our experiments. (iii) Accurate experimental measurements of absorbed fluence on ablation threshold and crater depth have been done. This is crucial for verification of model parameters. Good agreement of theory with experiments in both energy and geometry description has been achieved.

Acknowledgement The work is supported by the RFBR 07-02-00764.

References

1. E. Leveugle, D.S. Ivanov, L.V. Zhigilei, Appl. Phys. A **79**, 1643 (2004)
2. S. Eliezer, N. Eliaz, E. Grossman, D. Fisher, I. Gouzman et al., Phys. Rev. B **69**, 144119 (2004)
3. M.B. Agranat et al., JETP Lett. **85**(6), 271 (2007)
4. V. Temnov, PhD thesis, Univ. of Duisburg-Essen, 2004
5. S.I. Anisimov et al., J. Exp. Theor. Phys. **103**, 183 (2006)
6. S.I. Anisimov et al., Sov. Phys. JETP **39**, 375 (1974)
7. Y. Mishin et al., Phys. Rev. B **59**, 3393 (1999)
8. A.V. Bushman, G.I. Kanel', A.L. Ni, V.E. Fortov, *Intense Dynamic Loading of Condensed Matter* (Taylor & Francis, London, 1993)
9. V.V. Zhakhovskii et al., in *IEEE Proceedings of the 5th International Symposium on Cluster Computing and Grid (CCGrid 2005)*, vol. 2, 9–12 May 2005, pp. 848–854
10. E. Webb III, G. Grest, Phys. Rev. Lett. **86**, 2066 (2001)